Biosensors and Bioelectronics 143 (2019) 111634

Contents lists available at ScienceDirect

Biosensors and Bioelectronics

journal homepage: www.elsevier.com/locate/bios

Design of $Ni(OH)_2$ nanocages@MnO_2 nanosheets core-shell architecture to jointly facilitate electrocatalytic dynamic for highly sensitive detection of dopamine

Tong Yang[a,b], Liangliang Tian[a,b,*], Enmin Zhou[c], Gege He[d], Daidong Chen[a,b], Jinqiu Xie[a]

[a] *Research Institute for New Materials Technology, Chongqing University of Arts and Sciences, Chongqing, 400000, PR China*
[b] *Faculty of Materials and Energy, Southwest University, Chongqing, 400000, PR China*
[c] *School of Science, Chongqing University of Posts and Telecommunication, Chongqing, 400000, PR China*
[d] *School of Science, Xi'an Jiaotong University, Xi'an, Shanxi, 710000, PR China*

ARTICLE INFO

Keywords:
$Ni(OH)_2$ nanocages@MnO_2 nanosheets
Core-shell architecture
Coordinated etching and precipitation
Dopamine detection
Electrochemical sensing

ABSTRACT

In this work, $Ni(OH)_2$ nanocages@MnO_2 nanosheets core-shell architecture ($Ni(OH)_2$ NCs@MnO_2 NSs CSA) was successfully prepared through coordinated etching and precipitation (CEP) route followed by hydrothermal reaction, and then tested as sensitive electrode material for detection of dopamine (DA). The three dimensional (3D) hollow $Ni(OH)_2$ core effectively prevented the aggregation of MnO_2 NSs, leading to high utilization rate of MnO_2 NSs. Meanwhile, the two dimensional (2D) MnO_2 shell endowed $Ni(OH)_2$ NCs with larger specific area and abundant diffusion channels, facilitating mass transport. $Ni(OH)_2$ NCs@MnO_2 NSs CSA modified glassy carbon electrode (GCE) exhibited two satisfying sensitivities of 467.1 and 1249.9 μA mM^{-1} cm^{-2} within the two linear ranges of 0.02–16.30 μM and 18.30–118.58 μM, respectively. Furthermore, $Ni(OH)_2$ NCs@MnO_2 NSs CSA/GCE presented low detection limit of 1.75 nM and short response time of 1.14 s. Overall, $Ni(OH)_2$ NCs@MnO_2 NSs/GCE looks promising for analytical sensing of DA thanks to its prominent electrocatalytic dynamic issued from the 3D hollow structure@2D nanosheets core-shell architecture.

1. Introduction

Dopamine (DA) is a neurotransmitter with important functions in behavioral response and release of hormones. Some diseases, such as Parkinson, Schizophrenia and Huntington are closely related to DA levels (Kim et al., 2010). Therefore, accurate monitoring of DA concentrations is of great importance for human health and disease prevention. Due to the ultralow concentration (B.B. Yang et al., 2015a), sensors with high sensitivities and low detection limits are necessary for the accurate determination of DA. Electrochemical-based routes have attracted increasing attention due to simple operation, low cost, and high sensitivity (Yang et al., 2019). Since the performance of electrochemical sensors depends on properties of the working electrodes, the sensitive detection of DA can be achieved through rational design of electrocatalysts.

Transition metal oxides/hydroxides (TMOs/TMHs) have attracted lots of attention in electrocatalysis due to their low cost, high redox activity and excellent cycling stability (Liu et al., 2012). Inspired by kinetics, electrocatalytic activities of TMOs/TMHs closely correlate with the microstructure, such as morphology, surface area, and porosity. Hence, substantial efforts have been devoted to the design of TMOs/TMHs electrodes with improved microstructures (Long et al., 2018; Zhang et al., 2018). Thereinto, integration of materials with different dimensions is effective to construct TMOs/TMHs electrodes with high electrocatalytic activities. For example, MoS_2 nanosheets-coated CoS_2 nanowires have been synthesized to obtain high-performance towards hydrogen evolution reaction (Huang et al., 2015). Yang et al. synthesized $Ni(OH)_2$ nanoflakes modified polypyrrole nanowires with improved characteristics towards glucose detection (J. Yang et al., 2015b). These integrated nanoelectrocatalysts combined the advantages of different dimensional materials and overcame the structural shortcomings of each component thanks to synergetic effects.

Two dimensional (2D) nanosheets have unique physicochemical properties issued from high structural and morphologic anisotropies (Islam et al., 2018). The structural characteristics could create large specific surface areas, more exposing catalytic active sites and short transfer distances for both ions and electrons. However, 2D nanosheets are prone to agglomeration due to large contact areas between each

---

[*] Corresponding author. Research Institute for New Materials Technology, Chongqing University of Arts and Sciences, Chongqing, 400000, PR China.
E-mail address: tianll07@163.com (L. Tian).

https://doi.org/10.1016/j.bios.2019.111634
Received 25 June 2019; Received in revised form 11 August 2019; Accepted 24 August 2019
Available online 26 August 2019
0956-5663/ © 2019 Elsevier B.V. All rights reserved.

other, leading to low utilization of electrocatalyst. Direct deposition of 2D nanosheets on special scaffolds is effective to overcome such problems. Three dimensional (3D) hollow structures with large internal and external specific areas would provide numerous active sites and sufficient contact areas between the electrode and electrolyte. Moreover, ultrathin shell is beneficial for confined electron transfer, resulting in fast electron transfer rate. Thus, immobilization of 2D nanosheets on 3D hollow scaffold would effectively prevent aggregation of 2D nanosheets to make full use of the 2D materials (Li et al., 2017; Xia et al., 2016). Simultaneously, 2D shells endow 3D core with large specific areas and abundant diffusion channels, leading to improved mass transport dynamics. The unique 3D hollow core@2D shell structures have been reported in the field of electrochemistry. However, to the best of our knowledge, no studies of the unique structure were reported in electrochemical sensor so far. Most of the reported articles commonly employ hollow carbon scaffolds for 2D shell, such as carbon nanocages@MoS_2 nanosheets for lithium battery (Yu et al., 2015), MoS_2 nanosheets on hollow carbon spheres for supercapacitors (Liu et al., 2018) and hollow carbon spheres supported NiFe hydroxides nanosheets for oxygen evolution reaction (Ni et al., 2017). Although 3D hollow carbon scaffolds prevent the aggregation and make full use of the 2D shell, the electrocatalytic activity of general carbon materials towards DA is insufficient and limits the further promotion of the sensor. The substitution of high-active 3D hollow TMHs/TMOs for hollow carbon scaffolds not only utilizes the structural advantages of the unique structure, but also acquires higher electrocatalytic activity.

In this work, 3D $Ni(OH)_2$ nanocages were employed as a scaffold for 2D MnO_2 nanosheets for the first time to improve the electrocatalytic activities. $Ni(OH)_2$ nanocages@MnO_2 nanosheets core-shell architecture ($Ni(OH)_2$ NCs@MnO_2 NSs CSA) was synthesized by combining coordinated etching and precipitation (CEP) route with the hydrothermal reaction. MnO_2 shell composed of nanosheets was vertically grown on 3D cubic $Ni(OH)_2$ NCs to yield hollow hierarchical architectures. The integrated $Ni(OH)_2$ NCs@MnO_2 NSs CSA combined the structural and functional advantages of both $Ni(OH)_2$ NCs and MnO_2 NSs. The synergetic effect yielded $Ni(OH)_2$ NCs@MnO_2 NSs CSA modified glassy carbon electrode (GCE) with high sensitivity towards DA combined with low detection limit, acceptable reproducibility, and reasonable selectivity.

2. Experimental

2.1. Reagents

$CuCl_2 \cdot 2H_2O$, $NiCl_2 \cdot 6H_2O$, $Na_2S_2O_3 \cdot 5H_2O$, $KMnO_4$, polyvinylpyrrolidone (PVP, $M_w = 40000$) and NaOH were purchased from Chengdu Kelong Chemical Reagent Corporation. Glucose (Glu.), DA, lactose (Lact.), sucrose (Sucr.), fructose (Fruc.), L-ascorbic acid (AA), uric acid (UA) and Nafion solution (5 wt% in mixture of lower aliphatic alcohols and water) were all from Sigma-Aldrich.

2.2. Synthesis of $Ni(OH)_2$ NCs

The cubic Cu_2O templates were synthesized according to our previous work (Tian et al., 2014), and $Ni(OH)_2$ NCs were subsequently prepared through $S_2O_3^{2-}$ involved CEP route. Briefly, 400 mg Cu_2O and 140 mg $NiCl_2$ powders were poured into a 1000 mL beaker containing 400 mL water and alcohol at volume ratio of 1:1. After short ultrasonic treatment, 13.2 mg PVP was added to the mixture under stirring for 30 min. Then, 160 mL $Na_2S_2O_3$ (1 M) was added dropwise and the reaction last 3 h at room temperature. The products were collected by centrifugation and dried in vacuum at 60 °C for 12 h.

2.3. Synthesis of $Ni(OH)_2$ NCs@MnO_2 NSs CSA

$Ni(OH)_2$ NCs@MnO_2 NSs CSA was formed by hydrothermal reaction. Typically, 30 mg of $Ni(OH)_2$ NCs were dispersed in 30 mL $KMnO_4$ (0.02 M). After stirring for 30 min, the suspension was poured into a 50 mL stainless steel autoclave and maintained at 140 °C for 4, 8, and 12 h, respectively. The products were then washed and dried in vacuum at 60 °C for 12 h MnO_2 NSs were also obtained through hydrothermal reaction for 12 h without addition of $Ni(OH)_2$ NCs (see SEM image in Fig. S1).

2.4. Characterization

The crystal structures of the products were characterized by X-ray diffraction (XRD, Rigaku D/Max-2400) using Cu Kα radiation (40 kV, 60 mA). The compositions were analyzed by X-ray photoelectron spectroscopy (XPS, ESCALAB250Xi) with C 1s peak (284.8 eV) as internal standard. The morphologies were observed via field emission scanning electron microscopy (FESEM, SU8020) and high-resolution transmission electron microscopy (HRTEM, FEI F20) equipped with energy dispersive X-ray spectroscopy (EDX). The Brunauer-Emmett-Teller (BET, Belsort-max) method was utilized to measure the specific surface areas and pore structures.

2.5. Electrochemical measurements

All the electrochemical measurements were carried out in 0.1 M phosphate buffer solution (PBS, pH 7.0) on a μIII Autolab electrochemical workstation. The modified GCEs ($\Phi = 3$ mm) were used as working electrode, Ag/AgCl (saturated KCl) as reference, and Pt disk ($\Phi = 2$ mm) as counter electrode. The working electrodes were prepared by first polishing the GCEs by alumina slurry followed by ultrasonic cleaning in diluted HNO_3, water, and ethanol. Afterward, 5 mg of each active materials were dispersed in mixed 0.9 mL water and 0.1 mL Nafion solution. Then, 5 μL of the suspension was dropped onto pretreated GCE and left to dry at room temperature to yield $Ni(OH)_2$ NCs@MnO_2 NSs CSA/GCE, $Ni(OH)_2$ NCs/GCE and MnO_2 NSs/GCE, respectively.

3. Results and discussion

3.1. Characterization

A schematic illustration of the synthetic process of $Ni(OH)_2$ NCs@MnO_2 NSs CSA is displayed in Fig. 1a. In stage I, Ni^{2+} ions were concentrated on Cu_2O templates with the assistance of ultrasonic. The introduction of $S_2O_3^{2-}$ ions led to coordinated etching of Cu_2O and formation of soluble $[Cu_2(S_2O_3^{2-})x]^{2-2x}$ ions (Eq. (1)) due to soft interaction between Cu^+ and $S_2O_3^{2-}$ (Nai et al., 2013). Simultaneously, the combination of adsorbed Ni^{2+} and OH^- released from coordinated etching and partial hydrolyzation of $S_2O_3^{2-}$ (Eq. (2)) formed $Ni(OH)_2$ shell around Cu_2O templates (Eq. (3)). The mass transport played a critical role in the reaction process (Fig. 1b). The diffusion of $S_2O_3^{2-}$ from external to internal cavity represented the etching rate of Cu_2O, and transport of OH^- from interior to exterior was closely related to the generation of $Ni(OH)_2$ shell. The coordinated etching rate of Cu_2O templates and synchronous control of the precipitation rate of $Ni(OH)_2$ shell led to formation of well-defined $Ni(OH)_2$ NCs (stage II). Finally, $Ni(OH)_2$ NCs@MnO_2 NSs CSA was constructed through the wrapping of MnO_2 NSs by hydrothermal method (Eq. (4), stage III). Fig. 1c displays the TEM images of the products obtained at different stages. The observed formation process agreed well with above deduced mechanism. Fig. S2 provides SEM details of formation process of MnO_2 NSs. Obviously, MnO_2 nanoparticles issued from decomposition of $KMnO_4$ firstly aggregated onto $Ni(OH)_2$ NCs and then gradually grew to form MnO_2 NSs.

$$Cu_2O + S_2O_3^{2-} + H_2O \rightarrow [Cu_2(S_2O_3^{2-})x]^{2-2x} + 2OH^- \quad (1)$$

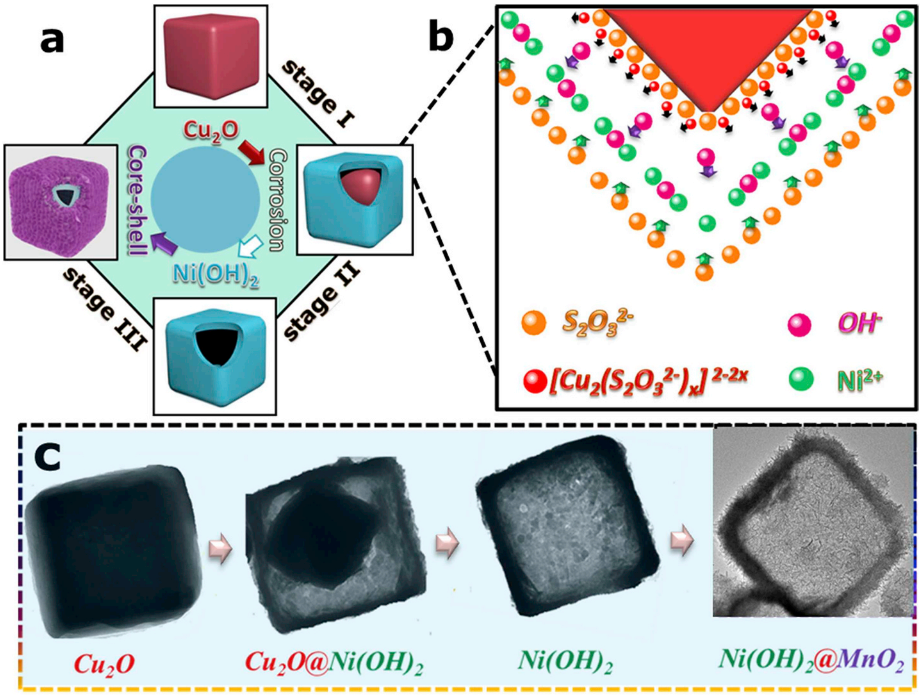

Fig. 1. (a) Schematic illustration of the synthetic process for $Ni(OH)_2$ NCs@MnO_2 NSs CSA; (b) The mass transport dynamic for CEP route; (c) TEM images of the samples obtained at different stages.

$$S_2O_3^{2-} + H_2O \rightarrow HS_2O^- + OH^- \qquad (2)$$

$$Ni^{2+} + 2OH^- \rightarrow Ni\,(OH)_2 \qquad (3)$$

$$KMnO_4 \rightarrow MnO_2 + O_2 \qquad (4)$$

The XRD pattern of $Ni(OH)_2$ NCs@MnO_2 NSs CSA is shown in Fig. 2a. The peak located at 38.7° can be indexed to typical hexagonal $Ni(OH)_2$ (PDF#14-0117). The characteristic peaks at 36.8° and 65.7° were assigned to the (006) and (119) planes of birnessite-type MnO_2 (PDF#18-0802). The detailed information on chemical compositions and electronic states was also investigated by XPS. Compared to Ni $(OH)_2$ NCs (Fig. S3), K and Mn were also visible in the survey spectrum, which was consistent with the EDS data (Fig. S4). For Ni 2p (Fig. 2b), two major peaks located at 854.76 eV and 857.39 eV with spin-energy separation of 17.68 eV were noticed and assigned to Ni $2p_{3/2}$ and Ni $2p_{1/2}$, respectively (Niu et al., 2015). The other two extra peaks were

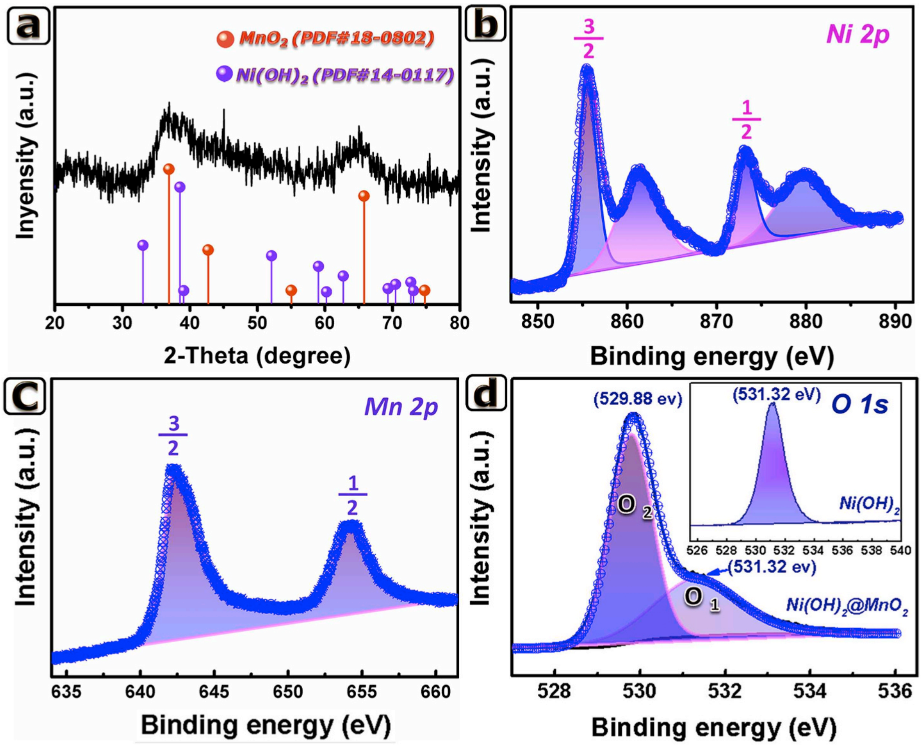

Fig. 2. (a) XRD pattern of $Ni(OH)_2$ NCs@MnO_2 NSs CSA; High-resolution XPS spectra for (b) Ni 2p, (c) Mn 2p and (d) O 1s.

identified as satellite peaks of Ni $2p_{3/2}$ and Ni $2p_{1/2}$, further confirming existence of Ni^{2+} in the products. In Mn 2p spectrum (Fig. 2c), two major peaks at 642.37 eV and 654.19 eV were obtained and indexed to Mn $2P_{3/2}$ and Mn $2P_{1/2}$ in Mn^{4+} levels, respectively (Huang et al., 2017). Besides, two different states of O_1 and O_2 were observed in the O 1s spectrum (Fig. 2d). Compared to O 1s spectrum of $Ni(OH)_2$ NCs (inset in Fig. 2d), the O_1 peak at 531.32 eV could be attributed to the hydroxyl groups in $Ni(OH)_2$. The O_2 peak at 529.88 eV might be assigned to oxygen atoms in MnO_2 (Li et al., 2018). In sum, XRD and XPS data both confirmed the successful preparation of $Ni(OH)_2/MnO_2$ composite.

As shown in Fig. S5, the Cu_2O templates displayed cubic morphology with average edge length around 500 nm. After CEP process, Ni$(OH)_2$ NCs still retained the cubic features (Fig. S6a). In inset of Fig. S6a, the broken cube displayed hollow interior structure, confirming the formation of cage-like architecture. Moreover, $Ni(OH)_2$ NCs depicted nearly the same edge length as Cu_2O templates (Fig. S6b). Ni$(OH)_2$ NCs illustrated tiny particles with rough porous surface (Fig. S6c), providing enough sites for further growth of MnO_2 NSs. In addition, $Ni(OH)_2$ NCs retained its cubic characteristics after the hydrothermal reaction (Fig. S6d). However, the nanocages surfaces became apparently rougher. Careful analysis showed MnO_2 layers vertically grown on $Ni(OH)_2$ NCs to form hollow core-shell structures (Fig. S6e). On the other hand, the reticular MnO_2 layer was composed of randomly assembled MnO_2 NSs (Fig. S6f). The hollow $Ni(OH)_2$ core provided enough external and internal surface area to promote effective adsorption of analytes. The 2D porous shell not only provided sufficient diffusion channels for the analytes but also improved the electron collection and transfer rate.

In Fig. 3a, the TEM image revealed $Ni(OH)_2$ NCs with well-defined cage-like morphologies. After the hydrothermal process, layered MnO_2 NSs were deposited on $Ni(OH)_2$ NCs without noteworthy interlayer gaps (Fig. 3b). The thicknesses of MnO_2 layer and $Ni(OH)_2$ NC were determined as 25 and 60 nm, respectively (Fig. 3c). The selected area electron diffraction (SAED) pattern revealed polycrystalline feature of MnO_2 NSs (inset of Fig. 3c). The lattice fringes of 0.24 nm, 0.17 nm and 0.14 nm were consistent with (006), (301) and (119) crystal planes of birnessite-type MnO_2 (PDF#18-0802) (Fig. 3d). The element distributions of $Ni(OH)_2$ NCs@MnO_2 NSs CSA were measured by Mapping and line scan EDX. In Fig. 3e, the signals of O, Mn and Ni elements were strong on the edge and weak in the center, confirming the characteristic of hollow structures (Wang et al., 2018). The line-scan data also confirmed concentrated near-surface distributions of Mn, Ni and O (Fig. 3f), which agreed well with the analysis of mapping. Overall, XRD, SEM and TEM data demonstrated the successful design of Ni$(OH)_2$ NCs@MnO_2 NSs CSA.

The surface area and porosity of each specimen were measured by BET method. The hysteresis loop of $Ni(OH)_2$ NCs@MnO_2 NSs CSA in Fig. 3g belonged to H4 type as typical characteristic of multi-layer structure (Zou et al., 2018). The surface area of $Ni(OH)_2$ NCs@MnO_2 NSs CSA was estimated to 50 $m^2\,g^{-1}$, hence much larger than those of $Ni(OH)_2$ NCs (22.1 $m^2\,g^{-1}$, Fig. 3h) and MnO_2 NSs (32 $m^2\,g^{-1}$, Fig. 3i). The mean pore size of $Ni(OH)_2$ NCs@MnO_2 NSs CSA was around 5.7 nm, and served as suitable channels for efficient mass transport. Moreover, the pore volumes of $Ni(OH)_2$ NCs@MnO_2 NSs CSA, Ni$(OH)_2$ NCs and MnO_2 NSs were recorded as 0.06, 0.03 and 0.031 $cm^3\,g^{-1}$, respectively. The large surface area, significant pore volume and suitable channels would benefit the electrocatalytic activity.

3.2. *Electrochemical performance of $Ni(OH)_2$ NCs@MnO_2 NSs CSA/GCE*

The electrochemical performances of $Ni(OH)_2$ NCs@MnO_2 NSs CSA/GCE were evaluated by cyclic voltammetry (CV), electrochemical impedance spectroscopy (EIS), and chronoamperometry (CA). In absence of DA, no peaks were observed in the CV curve (Fig. 4a). By comparison, obvious redox peaks were noticed in presence of 50 μM DA. For $Ni(OH)_2$ NCs/GCE (Fig. S7a) and MnO_2 NSs/GCE (Fig. S7b), the anodic currents increased after addition of DA but the intensities were lower than that of $Ni(OH)_2$ NCs@MnO_2 NSs CSA/GCE, indicating lower electrocatalytic activities. The electrocatalytic mechanism of DA is provided in Fig. 4b. The metal components in $Ni(OH)_2$ NCs@MnO_2 NSs CSA would provide electron mediators of Ni^{3+} and Mn^{4+}, which then will take away electrons from the adsorbed DA molecules to yield Ni^{2+} and Mn^{2+}. Simultaneously, DA molecules were oxidized to DA quinone (Salamon et al., 2015).

CV profiles of $Ni(OH)_2$ NCs@MnO_2 NSs CSA/GCE were recorded at different scan rates in Fig. 4c. As shown in the inset, both the anodic and cathodic peak currents linearly increased with square root of scan rate, revealing typical diffusion-controlled electrocatalytic processes (Mei et al., 2018). Additionally, the positive/negative shifts in anodic/cathodic peak potentials linearly depended on the logarithm of scan rate (Fig. 4d), indicating quasi-reversible electrocatalytic processes (Sun et al., 2013). Hence, the electron transfer number and coefficient can be calculated by the Laviron's equations (Laviron, 1979):

$$Epa = E^{0'} + 2.3\left(\frac{RT}{(1-\alpha)nF}\right)\lg\nu \tag{5}$$

$$Epc = E^{0'} - 2.3\left(\frac{RT}{\alpha nF}\right)\lg\nu \tag{6}$$

where n is number of electrons transferred, α is electron transfer coefficient, ν is the scan rate, and $E^{0'}$ is the formal potential. *F, R* and *T* have their traditional meanings. In.

Fig. 4d, the regression equations could be expressed as follow: $E_{pa} = 0.2495 + 0.08457\lg\nu$ ($R^2 = 0.992$) and $E_{pc} = 0.3095\text{-}0.06186\lg\nu$ ($R^2 = 0.994$). The values of n and α were calculated as 1.676 and 0.576, respectively, revealing fast two electrons transfer electrocatalytic processes.

The Nyquist plots of $Ni(OH)_2$ NCs@MnO_2 NSs CSA/GCE, Ni$(OH)_2$ NCs/GCE and MnO_2 NSs/GCE electrodes are gathered in Fig. 4e. As depicted in inset I, the equivalent circuit was fitted by electron transfer resistance (R_{ct}), solution resistance (R_s), and Warburg resistance (Z_W) (Tian et al., 2019). As shown in Table S1, $Ni(OH)_2$ NCs@MnO_2 NSs CSA/GCE presented smaller R_{ct} (0.139 kΩ) than Ni$(OH)_2$ NCs/GCE (1.56 kΩ) and MnO_2 NSs/GCE (2.05 kΩ). The low electron transfer resistance can be ascribed to the high electron collection efficiency and elevated electron transfer rate provided by the unique structure. In Inset II, $Ni(OH)_2$ NCs@MnO_2 NSs CSA/GCE exhibited lower Rs (0.105 kΩ) than $Ni(OH)_2$ NCs/GCE (0.163 kΩ) and MnO_2 NSs/GCE (0.147 kΩ). In addition, $Ni(OH)_2$ NCs@MnO_2 NSs CSA/GCE depicted larger Zw than $Ni(OH)_2$ NCs/GCE and MnO_2 NSs/GCE, revealing lower ion diffusion resistance. The lower ion diffusion resistance might be attributed to the 3D porous feature of $Ni(OH)_2$ scaffold and ample diffusion channels constructed by MnO_2 NSs (Fig. 4f). In sum, $Ni(OH)_2$ NCs@MnO_2 NSs CSA/GCE exhibited better mass transport and electron transfer dynamic advantages, leading to excellent electrocatalytic activity.

The *i-t* curves of $Ni(OH)_2$ NCs@MnO_2 NSs CSA/GCE, $Ni(OH)_2$ NCs/GCE and MnO_2 NSs/GCE at 0.35 V with and without 0.1 mM DA are depicted in Fig. S8a, S8b and S8c, respectively. The relationship between I_{cat} and $t^{-1/2}$ for $Ni(OH)_2$ NCs@MnO_2 NSs CSA/GCE is summarized in Fig. S8d. Accordingly, the diffusion coefficient (D) of DA can be calculated by the Cottrell's equation (Yin et al., 2018):

$$Iact = nFAD^{1/2}C0\pi^{-1/2}t^{-1/2} \tag{7}$$

where I_{cat} is the current in 0.1 mM DA, n represents the number of electrons transferred, F is the Faraday constant, A is the electrode area, C_0 is the substrate concentration, D is the diffusion coefficient, and t expresses the elapsed time. The value of D for $Ni(OH)_2$ NCs@MnO_2 NSs CSA/GCE was estimated to $2.43 \times 10^{-6}\,cm^2\,s^{-1}$, which is much larger than $Ni(OH)_2$ NCs ($1.21 \times 10^{-6}\,cm^2\,s^{-1}$, Fig. S8e) and MnO_2 NSs/GCE

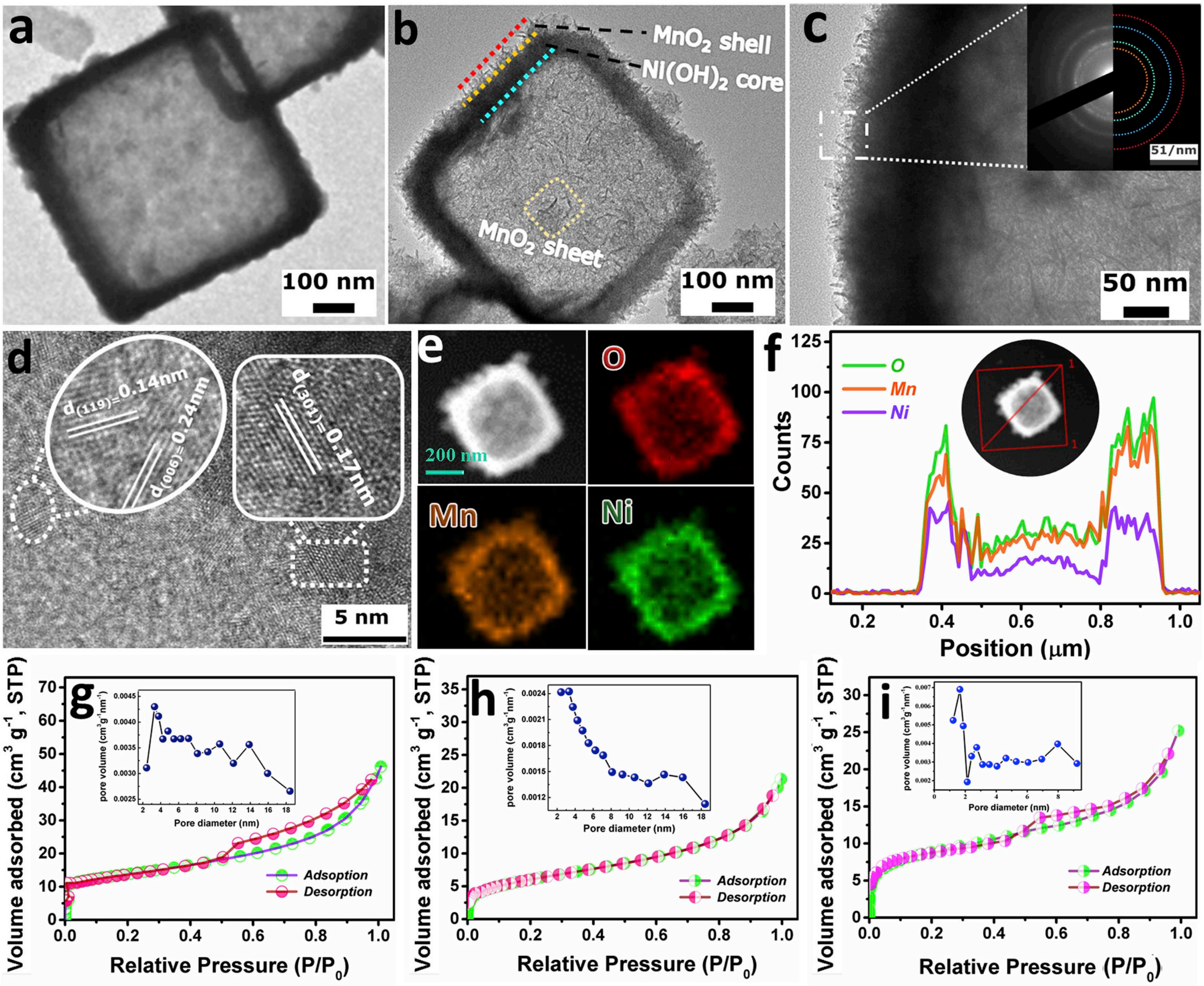

Fig. 3. TEM images of (a) $Ni(OH)_2$ NCs and (b, c) $Ni(OH)_2$ NCs@MnO_2 NSs CSA; Insert of Fig. 3c is the SAED pattern of MnO_2 NSs; (d) HRTEM image of MnO_2 NSs; (e) The element mapping and (f) line-scan EDX profile of $Ni(OH)_2$ NCs@MnO_2 NSs CSA; N_2 adsorption-desorption isotherms of (g) $Ni(OH)_2$ NCs@MnO_2 NSs CSA, (h) $Ni(OH)_2$ NCs and (i) MnO_2 NSs. Insets are the corresponding pore size distributions.

(2.44×10^{-9} cm^2 s^{-1}, Fig. S8f). The elevated value of D could be attributed to the 3D porous architecture and ordered channels formed by MnO_2 NSs. The catalytic rate constant (K_{cat}) was also calculated according to Eq. (8):

$$I\mathrm{act}/\mathrm{IL} = (\pi kcatC0t)^{1/2} \qquad (8)$$

where I_{cat} and I_L are the current in 0.1 mM and 0 mM DA, respectively, and K_{cat} is the catalytic rate constant. The k_{cat} value for $Ni(OH)_2$ NCs@MnO_2 NSs CSA/GCE was calculated as 1.7×10^3 M^{-1} s^{-1} (Fig. S8g), which was larger than $Ni(OH)_2$ NCs/GCE (0.25×10^3 M^{-1} s^{-1}, Fig. S8h) and MnO_2 NSs/GCE (0.41×10^3 M^{-1} s^{-1}, Fig. S8i). The elevated values of D and K_{cat} would lead to higher electrocatalytic activities.

3.3. Activity of $Ni(OH)_2$ NCs@MnO_2 NSs CSA towards detection of DA

To determine the optimal working potential, the *i-t* curves of $Ni(OH)_2$ NCs@MnO_2 NSs CSA/GCE were recorded at different potentials and the data are gathered in Fig. S9. $Ni(OH)_2$ NCs@MnO_2 NSs CSA/GCE showed higher response current at 0.35 V, which was selected as the optimal working potential. To evaluate the electrocatalytic activities, the *i-t* curves of $Ni(OH)_2$ NCs@MnO_2 NSs CSA/GCE, $Ni(OH)_2$ NCs/GCE and MnO_2 NSs/GCE at 0.35 V were recorded and the results are presented in Figs. S10a–c. Two linear ranges were clearly observed for all working electrodes (Fig. 5a). At low concentration, the electrocatalytic process was dominated by DA diffusion. The ultralow DA concentration caused insufficient utilization of active materials, especially the inner space, resulting in lower sensitivity. The active materials were thoroughly infiltrated at high DA concentration, leading to higher sensitivity (Fariba et al., 2017; Anees and Rajdip, 2014). The sensitivities, theoretically calculated detection limit, linear ranges and response time of all three electrodes are summarized in Table S2. The sensitivities of $Ni(OH)_2$ NCs@MnO_2 NSs CSA/GCE in low concentration range (0.02 μM to 16.3 μM) and high concentration range (18.3 μM to 118.58 μM) were recorded as 467.1 and 1249.9 μA mM^{-1} cm^{-2}, respectively. Obviously, the sensitivities of $Ni(OH)_2$ NCs@MnO_2 NSs CSA/GCE in both linear ranges were higher than those of $Ni(OH)_2$ NCs/GCE (399.2 and 665.3 μA mM^{-1} cm^{-2}) and MnO_2 NSs/GCE (43.9 and 498.1 μA mM^{-1} cm^{-2}). The higher electrocatalytic activity of $Ni(OH)_2$@MnO_2 CSA/GCE can be attributed to the synergistic effect between $Ni(OH)_2$ NCs and MnO_2 NSs. (1) Larger specific surface area was obtained through the coupling of $Ni(OH)_2$ NCs and MnO_2 NSs, which can be confirmed by the BET analysis; (2) $Ni(OH)_2$ NCs prevented the

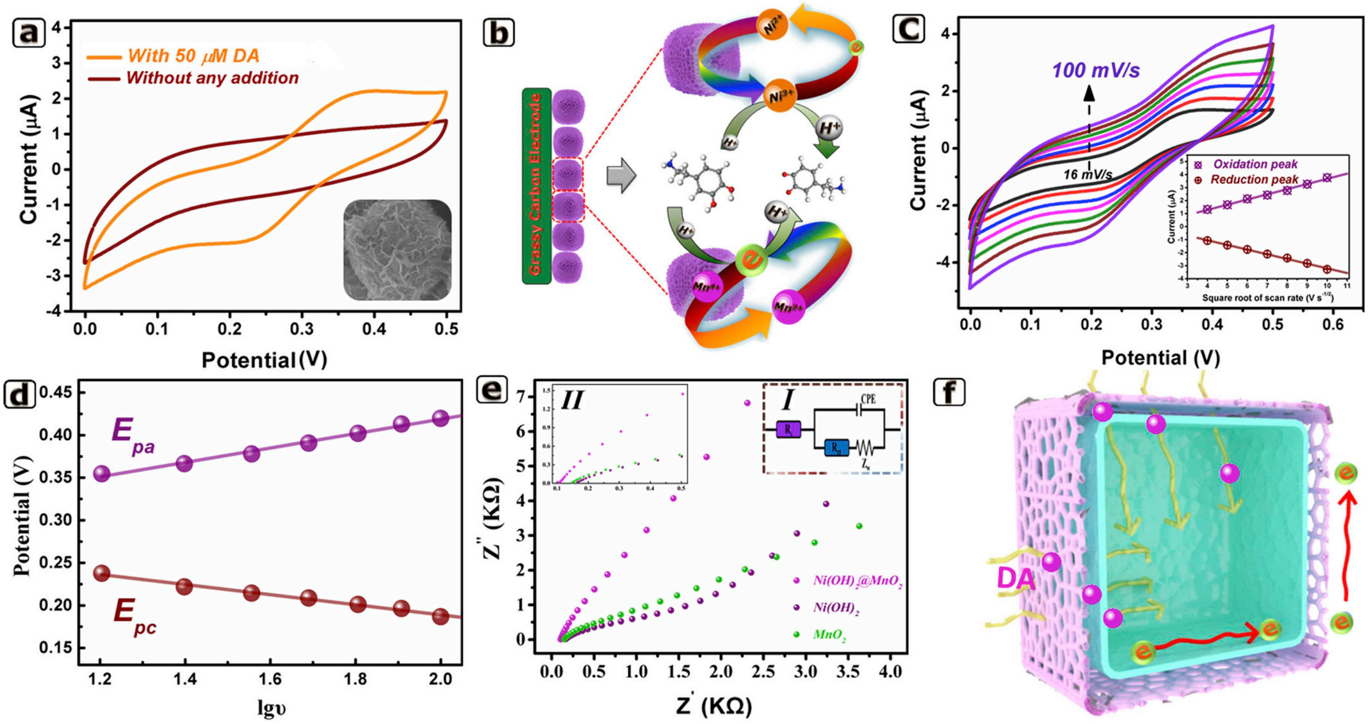

Fig. 4. (a) CVs of $Ni(OH)_2$ NCs@MnO_2 NSs CSA/GCE with and without 50 μM DA at 50 mV/s; (b) Schematic illustration of DA redox reaction on $Ni(OH)_2$ NCs@MnO_2 NSs CSA/GCE; (c) CVs of $Ni(OH)_2$ NCs@MnO_2 NSs CSA/GCE at different scan rates in 50 μM DA; Insert is the relationship between peak current and square root of scan rates; (d) Peak potentials versus lg*v*; (e) Nyquist plots of $Ni(OH)_2$ NCs@MnO_2 NSs CSA/GCE, $Ni(OH)_2$ NCs/GCE and MnO_2 NSs/GCE; (f) The illustration of dynamic advantages for $Ni(OH)_2$ NCs@MnO_2 NSs CSA.

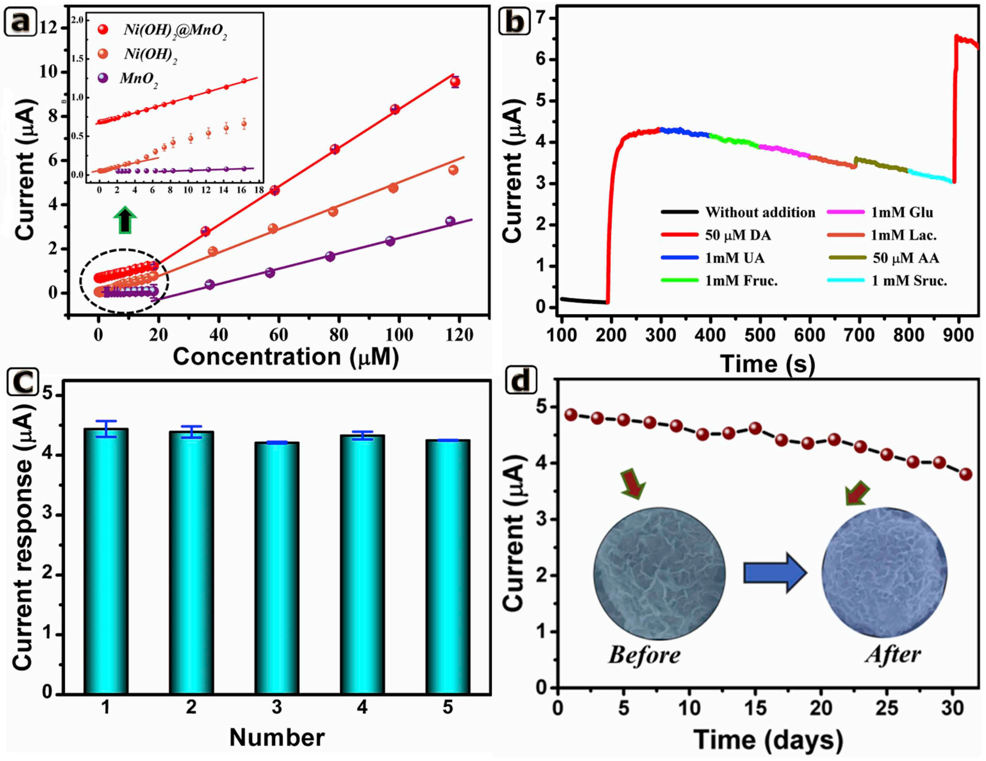

Fig. 5. (a) The relationship between DA concentration and response current of the three researched electrodes; (b) The selectivity measurement of $Ni(OH)_2$ NCs@MnO_2 NSs CSA/GCE with the successive addition of 1 mM UA, 1 mM Sruc., 1 mM Fruc., 1 mM Lac., 50 μM AA and 1 mM Glu at 0.35 V; (c) The response current of five $Ni(OH)_2$ NCs@MnO_2 NSs CSA/GCEs towards 50 μM DA; (d) Long-term stability of $Ni(OH)_2$ NCs@MnO_2 NSs CSA/GCE; Inset is the FESEM images of $Ni(OH)_2$ NCs@MnO_2 NSs CSA before and after electrochemical detection.

aggregation of MnO_2 NSs and made full use of the MnO_2 layer. The thin shell of $Ni(OH)_2$ NCs enhanced the transfer rate of catalytic electrons collected by MnO_2 layer; (3) MnO_2 NSs endowed $Ni(OH)_2$ NCs with amounts of diffusion channels and accelerated the transport of DA. This point was proved by above EIS analysis and *D* value calculation. Furthermore, $Ni(OH)_2$ NCs@MnO_2 NSs CSA/GCE presented much lower detection limit (1.75 nM, signal/noise = 3) than $Ni(OH)_2$ NCs/GCE (10.2 nM) and MnO_2 NSs/GCE (30.8 nM). Notably, $Ni(OH)_2$ NCs showed relatively higher sensitivity but longer response time, whereas MnO_2 NSs exhibited moderate sensitivity but shorter response time

Table 1
The detection of DA in DAI (n = 3).

Samples	Added(μM)	Founded(μM)	Recovery(%)	RSD (%)
1	5	4.87	97.4	1.3
2	10	9.56	95.6	2.2
3	50	46.02	92.0	4.1
4	100	101.74	101.7	0.9

(Table S2 and Figs. S11a–d). Hence, $Ni(OH)_2$ NCs mainly contributed to sensitivity but MnO_2 NSs was involved in response time. The performances of $Ni(OH)_2$ NCs@MnO_2 NSs CSA/GCE towards DA were compared with reported literatures shown in Table S3. Dramatically, $Ni(OH)_2$ NCs@MnO_2 NSs CSA/GCE presented lower detection limit than reported MnO_2 nanowires/chitosan-modified gold electrode (40 nM), β-MnO_2 nanorice (8.2 nM), Nafion/$Ni(OH)_2$/MWNTs/GCE (110 nM) and Au/m-$Ni(OH)_2$/GCE (320 nM), revealing that better electrochemical performance can be achieved through the coupling of $Ni(OH)_2$ NCs and MnO_2 NSs. In addition, $Ni(OH)_2$ NCs@MnO_2 NSs CSA/GCE displayed higher sensitivity than carbon-supported GO-MWCNT/MnO_2/AuNP/GCE (237 μA μM^{-1} cm^{-2}), demonstrating that the high-active $Ni(OH)_2$ NCs was superior as scaffold for MnO_2 compared to traditional carbon. Furthermore, $Ni(OH)_2$ NCs@MnO_2 NSs CSA/GCE displayed better electrochemical performance than other reports in terms of high sensitivity and low detection limit as shown in Table S3.

3.4. Selectivity, reproducibility, repeatability and stability

The selectivity of $Ni(OH)_2$ NCs@MnO_2 NSs CSA/GCE was tested by adding interfering species during *i-t* measurements (Fig. 5b) and only (4. 6±0.3)% interference current was observed for AA, indicating high selectivity. Moreover, the response current for the second addition of DA still retained 88% of its first injection. The attenuation in response current would be ascribed to the adsorption of trace interfering species or intermediate products on the electrode. To test the reproducibility, five $Ni(OH)_2$ NCs@MnO_2 NSs CSA/GCEs were prepared and their current responses towards 50 μM DA are recorded in Fig. 5c. The relative standard deviation (RSD) was determined as 2.8%, showing good reproducibility. The current responses of $Ni(OH)_2$ NCs@MnO_2 NSs CSA/GCE towards 25 μM DA were measured for 10 times (Fig. S12). The RSD was calculated as 1.1%, indicating outstanding repeatability. In terms of long-term stability, current responses towards 50 μM DA were recorded every two days for one month and the results are gathered in Fig. 5d. The last recorded response current still retained 82% of the initial value. In addition, the electrocatalyst still retained the unique core-shell architecture after 30 days (inset of Fig. 5d), suggesting remarkable stability.

3.5. Real sample detection

For practical applications, $Ni(OH)_2$ NCs@MnO_2 NSs CSA/GCE was used to detect DA in dopamine hydrochloride injection purchased from a local hospital. The tests were carried out according to the reported literature (Zou et al., 2018). The measured recovery was between 92% and 101.7% (Table 1). Furthermore, the RSD values were less than 4.1%, suggesting the promising application potential in enzyme-free DA electrochemical sensors.

4. Conclusions

In this work, 3D $Ni(OH)_2$ NCs@2D MnO_2 NSs core-shell structure was successfully prepared through CEP route followed by hydrothermal reaction. As a sensing electrode for DA, $Ni(OH)_2$ NCs@MnO_2 NSs CSA/GCE exhibited satisfactory sensitivities of 467.1 μA mM^{-1} cm^{-2} within the range of 0.02 μM–16.3 μM and 1249.9 μA mM^{-1} cm^{-2} within 18.3 μM–118.58 μM. An ultralow detection limit of 1.75 nM made this electrode attractive in electrochemical DA sensors. No more than (4. 6±0.3)% disturbing current was investigated in the presence of interfering species. The calculated D and K_{cat} for $Ni(OH)_2$ NCs@MnO_2 NSs CSA were 2.43×10^{-6} cm^2 s^{-1} and 1.7×10^3 M^{-1} s^{-1}, respectively. These remarkable electrocatalytic performances can be attributed to the highly porous structure, effective mass transport, and synergetic effect between $Ni(OH)_2$ NCs and MnO_2 NSs. Although better performance is achieved, electrode poisoning caused by the difficulties in desorption of intermediates still exists, resulting in relative narrower linear range. In the future research, interface modification can be introduced to make the active sites easier to regenerate and expand the working scope of the sensor.

CRediT authorship contribution statement

Tong Yang: Writing - original draft, Methodology. **Liangliang Tian:** Conceptualization. **Enmin Zhou:** Visualization, Investigation. **Gege He:** Resources, Supervision. **Daidong Chen:** Validation. **Jinqiu Xie:** Data curation, Supervision, Validation.

Declaration of competing interest

The authors declare that they have no known competing financial interests or personal relationships that could have appeared to influence the work reported in this paper.

Acknowledgements

We greatly appreciate the funding of National Natural Science Foundation of China (21403020), Basic and Frontier Research Program of Chongqing Municipality (cstc2016jcyjAX0014, CSTC2015JCYJBX0126, CSTC2016SHMSZX20001), Scientific and Technological Research Program of Chongqing Municipal Education Commission (KJ1601133, KJ1601104, KJ1711267) and Foundation of Chongqing University of Arts and Sciences (P2018CL07, M2017 ME19).

Appendix A. Supplementary data

Supplementary data to this article can be found online at https://doi.org/10.1016/j.bios.2019.111634.

References

Anees, Y.K., Rajdip, B., 2014. J. Electroanal. Chem. 727, 184–190.
Fariba, M., Karim, A.Z., Susana, C., Paloma, Y.S., José, M.P., 2017. Electrochim. Acta 246, 303–314.
Huang, J.L., Hou, D.M., Zhou, Y.C., Zhou, W.J., Li, G.Q., Tang, Z.H., Li, L.G., Chen, X.W., 2015. J. Mater. Chem. 3, 22886–22891.
Huang, M., Zhao, X.L., Li, F., Li, W., Zhang, B., Zhang, Y.X., 2017. J. Mater. Chem. 3 (24), 12852–12857.
Islam, M.S., Kim, M., Jin, X.Y., Oh, S.M., Lee, N.S., Kim, H., Hwang, S.J., 2018. ACS Energy Letters 3, 952–960.
Kim, Y.R., Bong, S., Kang, Y.J., Yang, Y., Mahajan, R.K., Kimc, J.S., Kim, H., 2010. Biosens. Bioelectron. 25 (10), 2366–2369.
Laviron, E., 1979. J. Electroanal. Chem. 101 (1), 19–28.
Li, J.H., Jiang, J.B., Liu, M.Q., Xu, Z.F., Deng, P.H., Qian, D., Tong, C.Y., Xie, H.B., Yang, C.M., 2017. Anal. Chim. Acta 985, 155–165.
Li, K.Z., Li, S.K., Huang, F.Z., Yu, X.Y., Lu, Y., Wang, L., Chen, H., Zhang, H., 2018. Nanoscale 10 (5), 2524–2532.
Liu, X.H., Ma, R.Z., Bando, Y.S., Sasaki, T., 2012. Adv. Mater. 24 (16), 2148–2153.
Liu, W.W., Zhu, M.H., Liu, J.H., Hu, W.J., Li, X., Liu, J., 2018. Inorg. Chem. Front 5, 2198–2204.
Long, X., Wang, Z.L., Xiao, S., An, Y.M., Yang, S.H., 2018. Mater. Today 19, 213–226.
Mei, X.R., Wei, Q.P., Long, H.Y., Yu, Z.M., Deng, Z.J., Meng, L.C., Wang, J., Luo, J.T., Lin, C.T., Ma, L., Zhe, K.Z., Hu, N.X., 2018. Electrochim. Acta 271, 84–91.
Nai, J.W., Tian, Y., Guan, X., Guo, L., 2013. J. Mater. Chem. Soc. 135 (43), 16082–16173.
Ni, Y.M., Yao, L.H., Wang, Y., Liu, B., Cao, M.H., Hu, C.W., 2017. Nanoscale 9 (32), 11596–11604.
Niu, H., Zhou, D., Yang, X., Li, X., Wang, Q., Qu, F.Y., 2015. Electrochim. Acta 3 (36), 18413–18420.
Salamon, J., Sathishkumar, Y., Ramachandran, K., Lee, Y.S., Yoo, D.J., Kim, A.G., Kumar,

G., 2015. Biosens. Bioelectron. 65, 269–276.
Sun, W., Cao, L.L., Deng, Y., Gong, S.X., Shi, F., Li, G.N., Sun, Z.F., 2013. Anal. Chim. Acta 781 (9), 41–47.
Tian, L.L., Zhong, X.H., Hu, W.P., Liu, B.T., Li, Y.F., 2014. Nanoscale Res. Lett. 9 (1), 68–72.
Tian, L.L., Xia, K.D., Wu, S.P., Cai, Y.H., Liu, H.D., Jing, X.L., Yang, T., Chen, D.D., Bai, X., Zhou, M., Li, L., 2019. Electrochim. Acta 307, 310–317.
Wang, S.b., Guan, B.Y., Lou, X.W., 2018. Energy Environ. Sci. 11 (12), 306–310.
Xia, Y., Wang, B.B., Zhao, X.J., Wang, G., Wang, H., 2016. Electrochim. Acta 187, 55–64.
Yang, B.B., Wang, J., Bin, D., Zhu, M.S., Yang, P., Du, Y.K., 2015a. J. Mater. Chem. B 3 (37), 7440–7448.
Yang, J., Cho, M., Pang, C.Y., Lee, Y.W., 2015b. Sens. Actuators, B 211, 93–101.
Yang, J., Hu, Y., Li, Y.C., 2019. Biosens. Bioelectron. 135, 224–230.
Yin, D., Bo, X.J., Liu, J., Guo, L.P., 2018. Anal. Chim. Acta 995, 11–20.
Yu, X.Y., Hu, H., Wang, Y.W., Chen, H.Y., Lou, X.W., 2015. Angew. Chem. Int. Ed. 54, 1–5.
Zhang, Q.B., Wang, J.X., Dong, J.C., Ding, F., Li, X.H., Zhang, B., Yang, S.H., Zhang, K.L., 2018. Nano Energy 13, 77–91.
Zou, G.Q., Hou, H.S., Zhao, G.G., Ge, P., Yin, D.L., Ji, X.b., 2018. J. Mater. Chem. 6 (11), 4839–4847.